Appl Phys B (2011) 105:793–800
DOI 10.1007/s00340-011-4543-y

Applied Physics B
Lasers and Optics

Lensing effects in Q-switched unstable laser cavities with side-pumped Nd:YAG and ruby crystal rods

D. Škrabelj · M. Gorjan · I. Drevenšek-Olenik · M. Marinček

Received: 2 February 2011 / Revised version: 9 March 2011 / Published online: 13 May 2011

Abstract We present a comprehensive numerical model that accounts for non-uniform pumping and a related thermal and electronic lensing effects in Q-switched unstable laser cavities. We study the influence of these effects on the output beam profile in Nd:YAG and ruby laser systems with side-pumped crystal rods. We also constructed both lasers to experimentally validate the numerical results and found very good agreement. The results show that both types of lensing effects are particularly detrimental in ruby, while they are insignificant in Nd:YAG.

1 Introduction

Q-switched unstable laser cavities provide certain advantages over the more common stable laser cavity types [1]. They allow for near diffraction-limited beams from cavities with large Fresnel numbers and at the same time preserve the energy extraction efficiency comparable to stable cavities [2]. Flashlamps or laser diodes can be used as pump sources, but specially the former are still considered to be the best in providing with high energy and good quality output beams that are needed e.g. for the LIDAR [3] and frequency conversion [4, 5]. Some applications (e.g. medical) require homogeneous (top-hat) beam profile. This can be best realized by employing a variable reflectivity mirror (VRM), i.e. a mirror with a super-Gaussian reflectivity profile, as an output coupler in an unstable cavity [2, 6, 7].

In high power lasers there is always present thermal lensing which was thoroughly studied for stable cavities, e.g. in [8]. On the contrary the studies were very rare for unstable laser cavities. The venerable formula of Koechner [9] was recently revised in [10], but it only accounts for the spherical lens effects assuming an azimuthal symmetry. The spherical lens can be successfully compensated for [11, 12], but such simplification may not always be justified because of the non-uniform pumping. The resulting cylindrical aberrations were studied in stable cavities with Nd:YAG laser rod [13–15]. A general description of the thermal effects is a three-dimensional problem and in order to solve for the temperature field one needs to know the absorbed pump power density. The pump absorption can be modeled effectively by ray-tracing and then considered as the heat source, which was done e.g. for the Nd:YAG [16, 17], Ti:sapphire [18] in stable cavities, and also for Yb:YAG slab lasers [19].

In certain laser materials, however, in addition to the thermal lensing there is also present an electronic population lensing effect. How the latter affects the laser beam generation was first studied in [24] for the Gaussian beam in a plano-concave stable cavity using a numerical model. Our recent study in [25] has revealed how the electronic population lensing affects the beam generation in unstable cavities. We have found that the influence of the population lens is much greater in unstable cavity compared to the stable cavity, i.e. the beam profile is greatly distorted and the energy fluctuates substantially from pulse to pulse.

While we have investigated only a single-shot regime in the previous work, we focus here on the thermal effects in

D. Škrabelj (✉) · M. Gorjan · M. Marinček
Fotona d.d., 1210 Ljubljana, Slovenia
e-mail: dejan.skrabelj@fotona.com

D. Škrabelj · I. Drevenšek-Olenik · M. Marinček
Complex Matter Department, Jožef Stefan Institute,
1000 Ljubljana, Slovenia

M. Gorjan · I. Drevenšek-Olenik
Faculty of Mathematics and Physics, University of Ljubljana,
1000 Ljubljana, Slovenia

addition to the population lensing effect. We simulate the beam generation in the laser cavity using a FFT-based numerical model of the electromagnetic (EM) field evolution inside the Q-switched laser cavity. We incorporate in this model both the thermal astigmatic and electronic population lenses. To approximate the thermal lens we first model the process of the pump absorption by ray-tracing and use it in the heat equation as a heat source. Then we solve the heat equation and determine the parameters of the effective thermal astigmatic lens from the temperature field. The electronic population lens is on the other hand incorporated directly in the numerical model of the laser cavity.

We model the performance of two unstable laser cavities with two distinctly different laser media: Nd:YAG and ruby ($Cr:Al_2O_3$). By investigating the combination of both lensing effects we found that ruby possesses pronounced thermal and also population lensing effects [20, 22], while they are much less significant in the Nd:YAG [23]. We have experimentally validated the numerical models by measurements on both Nd:YAG and ruby laser systems and found a very good agreement in both cases.

2 Description of the model

2.1 Laser cavity

The model of Q-switched laser cavity combines the EM field propagation with the laser amplification inside the crystal rod. The propagation is based on diffraction and is computed in Fourier space using the FFT algorithm, while the amplification is described by the common rate-equations.

A transversal profile of the EM field inside the cavity is represented by $n \times n = 256 \times 256$ mesh points lying in the x–y plane, which is perpendicular to the cavity axis z. The EM field propagates between 5 effective cavity planes as depicted in Fig. 1 and the field profile is calculated in each plane. We have used two counter-propagating EM fields to obtain better temporal resolution. The first plane represents an out-coupling mirror, the second and the fourth planes describe laser rod ends, the third is the center of the laser rod associated with optical amplification and the fifth plane is the back mirror with a Q-switch element.

The propagation of EM field between consecutive planes is calculated in the Fourier space. The spatial spectrum of the EM field in a selected plane, which is computed with the 2D FFT algorithm, is transformed to the next plane by multiplication with the transfer function of the free space. The 2D inverse FFT is then used to transform the propagated spatial spectrum back to the EM field in the real space.

The first plane represents the super-Gaussian mirror that partially reflects light back into the cavity, while the remaining part represents the laser output. The amplitude is modified according to the radial-dependent reflectance profile

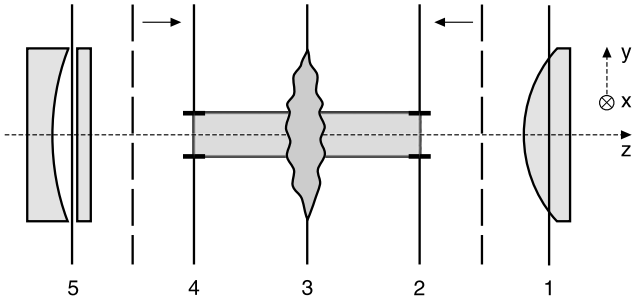

Fig. 1 Schematic drawing of the five computational planes in the laser cavity model. Plane *1* represents the out-coupling mirror, planes *2–4* describe the laser rod, and plane *5* describes the Q-switch element and the back cavity mirror. Two counter-propagating EM field wavefronts are drawn by *dashed lines*

$R(r) = R_0 e^{-2(r^2/w^2)^m}$, where $r = \sqrt{x^2 + y^2}$. The R_0 is the central reflectance, w is the width of the profile, and m is the super-Gaussian order. The phase of the reflected field is modified by the factor $e^{-ikr^2/R}$, where R is the radius of curvature of the mirror and k is the wave-number of the laser light.

In the second and the fourth plane, a spherical aperture describes the diffractive losses caused by the finite diameter of the laser rod. The edge of the aperture is smoothed in order to prevent the artificial diffraction.

Optical amplification occurs in the third plane and is described by the rate equations [8]. They couple the photon density Φ with the population inversion density N in the laser medium:

$$\frac{\partial \Phi}{\partial t} = \left(\sigma c N \frac{l}{l_c} - \frac{\Lambda}{t_0}\right)\Phi, \tag{1}$$

$$\frac{\partial N}{\partial t} = -\sigma c \Phi \gamma N, \tag{2}$$

where σ is the stimulated emission cross-section, c is the speed of light in the laser rod, l is the length of the laser rod, l_c is the length of the cavity, Λ denotes the internal cavity losses and $t_0 = 2l_c/c$ is the round-trip time of the EM field inside the cavity. The factor γ is equal to $1 + g_2/g_1$ with g_2/g_1 being the ratio between the upper and the lower laser level degeneracies.[1] Because the stimulated emission affects only the amplitude of the EM field $|E|$, but preserves its phase, the value of $|E|$ is transformed into Φ before solving the rate equations. Both quantities are related as $|E| \propto \sqrt{\Phi}$. After the amplification Φ is transformed back to $|E|$. New values of the EM field amplitude $|E|$ and inversion density N for each mesh point are calculated from (1) and (2) using the fourth-order Runge–Kutta method with the time-step of $t_0/2$, which corresponds to the half of the cavity round-trip time. To account for the spontaneous emission the phase

[1] In a four-level laser system $\gamma = 1$ and in a three-level laser system $\gamma > 1$.

of the incident field is slightly modified by addition of a phase noise to the EM field. The effects of the thermal and the electronic population lenses are taken into account in this plane by multiplying the EM field by the phase factors which will be given later.

In the fifth plane the phase of the EM field is altered by the curvature of the back mirror. The electro-optical Q-switch element is modeled with the conventional time-dependent transmission function taken from [8], which modifies the amplitude of the EM field. After the reflection at the back mirror, the EM field goes back through all the cavity planes in the reversed order.

The computation of the EM field starts in the central plane of the laser rod by generating matrix elements with unity amplitude and randomly distributed phases, while the initial population inversion density $N(t = 0)$ is the model input parameter. Such initialization simulates a real laser system in which the lasing process starts from the spontaneous emission. The major advantage of this approach is that no preferred symmetry is imposed on the generating laser beam.

2.2 Pump absorption

To calculate the absorption profile in the laser rod we constructed a model with a commercial ray-tracing software (Zemax-EE). The absorption spectra of the laser crystals were taken from [8] and the flashlamp emission spectra were taken from manufacturer's guide (Heraeus). We divided the absorption spectrum into eight sections to cover the full absorption dynamics. In this way we have taken into account that the low absorption sections result in a more uniform pumping, while the high absorption sections result in pumping of only the outer rim of the rod.

We took into consideration the detailed pumping geometry of the experimental setup: the Nd:YAG rod was 0.9% at. doped and had a diameter of 10 mm and a length of 100 mm, while the ruby rod was 0.03% wt. doped and had a diameter of 8 mm and a length of 114 mm. The laser crystal rods were enclosed in a close-coupled reflector made of diffuse ceramics together with two xenon-filled flashlamps in a plane arrangement as depicted in Fig. 2. We assumed a Lambertian scattering profile of the pump reflector with 99% reflectivity. We found out that it is also very important to include a proper scattering function of the matted laser rods as well as to take into account the surrounding water having an index of refraction of 1.33. In order to obtain the scattering function we have performed a separate experiment by directing a collimated He–Ne beam on one side of the laser rod perpendicular to its optical axis and we observed the scattered beam profile on the adjacent screen on the other side of the rod. We did not measure the function explicitly, but we instead replicated the experiment in the ray-tracing computer

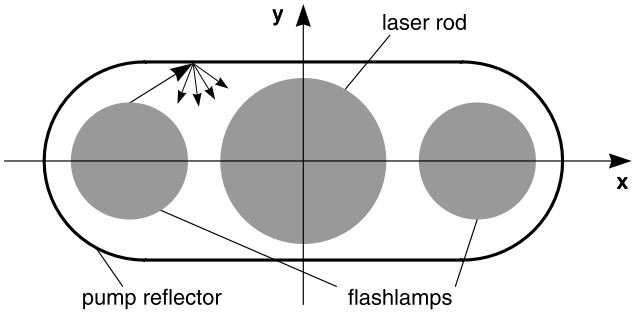

Fig. 2 Laser head cross-section of Nd:YAG and ruby lasers that was used in the pump absorption model

model, and thus we determined that a Gaussian scattering function with a variance of 0.1 produces the closest match with the experiment.

The ray-trace calculations were performed in 3D to also account for the skewed rays, but the resulting pump absorption profile was found to be essentially 2D with a small exception on both ends of the rod. Because of this we were using only the 2D absorption profile from the center of the rod to determine the phase factor of the thermal lens. The pump absorption profile looks almost identical to the temperature profile immediately after the first pump pulse, and the latter is shown in Fig. 3b.

2.3 Temperature profile

The calculated profile of the absorbed pump power was taken into account as an internal heat source in a 2D heat equation

$$D\nabla^2 T = \frac{\partial T}{\partial t} - \frac{q}{\rho c_p}, \tag{3}$$

where D is the thermal diffusivity constant defined as $D \equiv \kappa/\rho c_p$, with κ being the thermal conductivity, ρ the density and c_p the specific heat capacity of the laser material, and q is the power density of the heat source. We determined the latter using the calculated pump absorption profile and the estimated 20% efficiency of conversion of the applied electrical to absorbed pump energy. We measured the electrical energy using the experimental setup from Sect. 4; the pulse energies were 400 J and 60 J, and the pulse durations were 2.1 ms and 160 µs for the ruby and the Nd:YAG laser system, respectively. The boundary condition is applied along the rim of the rod as

$$\kappa(\mathbf{n} \cdot \nabla T) = h(T - T_w), \tag{4}$$

where h is the heat transfer coefficient, T_w is the surrounding water temperature, and $\mathbf{n}$ is the normal to the rod's surface. The values of the optical and thermal constants that we used in our calculations are given in Table 1.

Table 1 Values of the optical and thermal constants were taken from [8]

Constant	Unit	Nd:YAG	Ruby
n	1	1.82	1.76
dn/dT	$10^{-6}\,\mathrm{K}^{-1}$	7.6	12.6
D	$10^{-6}\,\mathrm{m}^2\,\mathrm{s}^{-1}$	4.8	14
κ	$\mathrm{W\,m}^{-1}\,\mathrm{K}^{-1}$	13	42
ρ	$\mathrm{kg\,m}^{-3}$	4560	3980
c_p	$\mathrm{J\,kg}^{-1}\,\mathrm{K}^{-1}$	590	753
h	$\mathrm{W\,m}^{-2}\,\mathrm{K}^{-1}$	5000	5000
τ	s	2.9	1.1

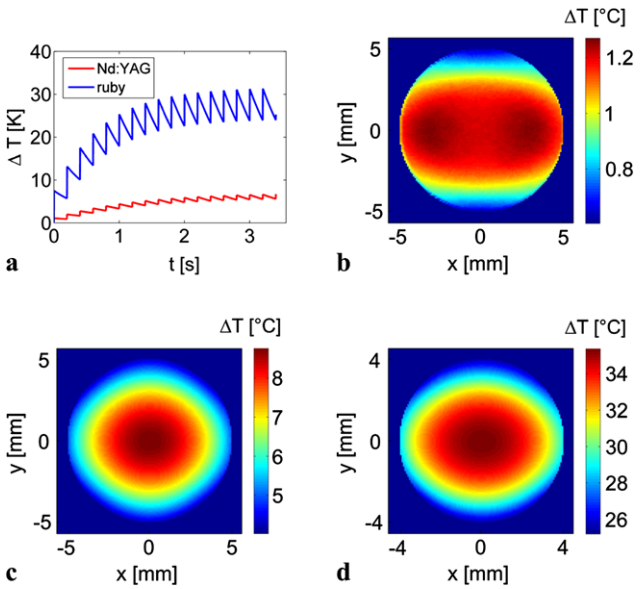

Fig. 3 Calculated temperature profiles in the laser rods pumped at the repetition rate of 5 Hz. (**a**) Time-dependent average temperature over the whole profile. (**b**) Temperature profile after the first pulse looks identical in both systems. (**c**) Temperature profile in Nd:YAG at $t = 3$ s. (**d**) Temperature profile in ruby at $t = 3$ s

We obtained the time-dependent solution of (3) and (4) using the finite element method (FEM). The time-dependent average temperature of the laser rod is shown in Fig. 3a at the repetition rate 5 Hz. It takes some time to reach the quasi steady-state when the incoming pump power equals the outgoing heat flow to the surrounding coolant. This time can be estimated from the laser rod's radius r_0 and its thermal diffusivity constant D by the thermal time constant $\tau \equiv r_0^2/D$, and its values are given in Table 1 for both laser rods. The temperature rises steeply after each pump pulse followed by a partial relaxation until the next pulse, and these oscillations remain in the quasi steady-state regime. The large difference in the quasi steady-state temperature of both laser media is associated with much more powerful pumping of the ruby, which is needed due to its three-level nature.

The temperature profile after the first pump pulse in Nd:YAG is shown in Fig. 3b and it completely reflects the absorbed pump power profile obtained from the ray-tracing (not shown). At initial stages there is no notable difference between the temperature profiles of the two laser media, except for the much higher average temperatures established in ruby. The single-shot profile is mainly determined by the pump absorption conditions as the thermal relaxation effects take much longer to arise. Since the pump conditions in both lasers are similar, i.e. the pump reflector design and the rod's surface scattering function, this also translates in very similar single-shot temperature profiles. However, the difference becomes apparent in the quasi steady-state regime. The steady-state temperature profile of the Nd:YAG rod pumped at 5 Hz is shown in Fig. 3c. Its shape exhibits almost a complete azimuthal angular symmetry and a parabolic radial dependence. In contrast, the steady-state temperature profile of the ruby rod pumped at 5 Hz has a considerable broken angular symmetry (Fig. 3d). The isotherms take an elliptical shape, which consequentially gives rise to the thermal astigmatic lensing effect. The eccentricity of the elliptical temperature profile is significant in ruby at 5 Hz and quite insignificant in Nd:YAG at 5 Hz, where the former better preserves the shape of the pump absorption profile. The basic reason for this difference lies in the difference between the thermal time constants of the two rods.

2.4 Thermal and electronic population lensing

The thermal lensing effect arises due to the changes in the index of refraction n induced by the temperature increase in the laser rod [8], denoted as dn/dT. We did not use the calculated temperature profile directly, but we have employed the fact that the actual profiles take elliptical shapes. Thus we have modeled the thermal astigmatic lens by superposition of the spherical part and inclusion of an additional refractory power in y-direction. The resulting phase factor for the propagation of EM field through such a lens is given as

$$\varphi_{t.l.} = e^{ik\frac{x^2+y^2}{2f_s}} e^{ik\frac{y^2}{2f_a}}, \tag{5}$$

where k is the wave vector, and f_s and f_a are the spherical and additional astigmatic focal lengths. We have applied (5) in the laser cavity model and it has proved to be very good for both laser media. Such description, however, only applies in the repetitive regimes and is not the best for the single-shot regime, but it can still provide a general representation of the astigmatism.

The dioptric power of both the spherical and the aspherical parts increases linearly with increasing average pump power. But the amount of astigmatism, i.e. the ellipticity of the isotherms on the temperature profile after the pumping pulse, is also a function of the pump repetition frequency

ν_{rep}. Our calculations show that some ellipticity is present at low repetition rate ($\nu_{\text{rep}} \ll 1/\tau$) where most of the pumping heat is driven away so that the temperature profile after each pulse is reminiscent of the single-shot regime. At mid repetition rate ($\nu_{\text{rep}} \sim 1/\tau$) there is enough buildup of the parabolic temperature profile that the elliptic shape becomes obscured, and at high repetition rate ($\nu_{\text{rep}} \gg 1/\tau$) the ellipticity emerges again due to the consecutive pulses coming too fast to allow for enough relaxation to the parabolic shape.

Electronic population lensing effect is most notable in the crystals doped with the ions of transition-metals as such ions lack the electronic shielding of the upper laser level. In this kind of materials the excitation of the higher energy levels causes applied internal strain that induces changes in the index of refraction [8]. Population lens distorts the phase of the evolving EM field in the laser cavity and vice versa. The amplification of the EM field depletes the gain medium which results in modified phase factor of the population lens. The population lens influences back the evolving EM field and therefore the population inversion. The effect of the population lens on the EM propagation is described by the phase factor

$$\varphi_{p.l.} = e^{ikC\frac{N}{N_0}l}, \tag{6}$$

where N is density of the inverted population, N_0 is number density of the active ions and l is the length of the rod. The population lensing effect of a laser medium is quantified by the coupling constant C.

The influence of the population lens on the laser pulse depends both on the value of the coupling constant and also on the type of the laser cavity. We recently analyzed the role of the population lens in an unstable super-Gaussian cavity [25] in the single-shot regime. The results showed distortions of the output laser beam in the near-field (NF) as well as in the far-field (FF). In addition, we showed that the output energy fluctuates from pulse to pulse and the efficiency of the laser is decreased because of the population lensing effect. We also included in the analysis a stable multimode plano-concave cavity and found that the distortions of the profile and energy fluctuations are much less significant there. The extent of the population lens' influence on the output laser pulse depends on the magnitude of the coupling constant C. The measured values of the constant in ruby range from $3.6 \cdot 10^{-6}$ to $2 \cdot 10^{-5}$ and there was no agreement about its sign in [20–22]. We have determined the constant to have a value between $7 \cdot 10^{-6}$ and $9 \cdot 10^{-6}$ and a positive sign [25].

3 Numerical results

We modeled both Nd:YAG and ruby laser media in Q-switched unstable cavity with super-Gaussian mirror. It turns out that ruby is a far more complicated system than Nd:YAG, so the majority of the results are for the former, while the latter serves more or less as a reference.

The Nd:YAG cavity was comprised of HR back mirror and a super-Gaussian output coupler set 500 mm apart and with radii of curvature $R_1 = 7$ m and $R_2 = -3.2$ m, respectively. The super-Gaussian mirror for Nd:YAG had the width of the reflectance profile $w = 3.0$ mm, the order $m = 4$, and the central reflectance $R_0 = 0.2$. The ruby cavity was also comprised of HR back mirror and a super-Gaussian output coupler. In this case the cavity length optical was 440 mm and the radii of curvature of the mirrors were $R_1 = 8$ m and $R_2 = -2.8$ m, respectively. The super-Gaussian mirror parameters for the ruby were: $w = 3.2$ mm, $m = 3$, and $R_0 = 0.53$.

The Nd:YAG rod had a doping concentration of 0.9% at., which translates to the number density of Nd ions $N_0 = 1.24 \cdot 10^{20}$ cm^{-3}. The stimulated emission cross-section is $\sigma = 2.8 \cdot 10^{-19}$ cm^2 at the emission wavelength of 1064 nm and $\gamma = 1$. The ruby rod had a doping concentration of 0.03% wt., which translates to the number density of Cr ions $N_0 = 9.46 \cdot 10^{18}$ cm^{-3}. The stimulated emission cross-section is $\sigma = 2.5 \cdot 10^{-20}$ cm^2 at the emission wavelength of 694 nm, and the value of γ is 2 because of the three-level operation of the ruby system. All other material constants were taken from Table 1.

The initial population inversion was set to $N = 0.01 \cdot N_0$ for Nd:YAG and $N = 0.66 \cdot N_0$ for ruby. The calculated pulse energies resulting from these initial excitations are 1000 mJ and 300 mJ for Nd:YAG and ruby, respectively. Both values are in good agreement with the pulse energies obtained from the experiments. The much larger initial population inversion in the ruby which nevertheless gives a much lower output energy is due to the three-level nature. The obtained beam caustics are depicted in Fig. 4 for ruby laser, where the effects of the astigmatic thermal lens can be observed.

3.1 Thermal lens

The ellipticity of the thermal profile in Nd:YAG operating at the repetition rate of 5 Hz is relatively low as can be seen in Fig. 3c. Consequently in our calculations we set the astigmatic part of the focal length $f_a \to \infty$. The spherical part of the focal length f_s is a function of the time-averaged pump power and thus also of the repetition rate. The magnification of the Nd:YAG cavity is about 1.8 and the coordinates in g-space are (1.17, 0.92) and both were found to be pretty much insensitive to the pumping power, i.e. the value of f_s. The calculated NF and FF beam profiles for single-shot regime ($f_s = \infty$) and at the repetition rate of 5 Hz ($f_s = 22$ m) are shown in Fig. 5. The NF profile remains largely unaffected, while in the FF profile a central dent is present in

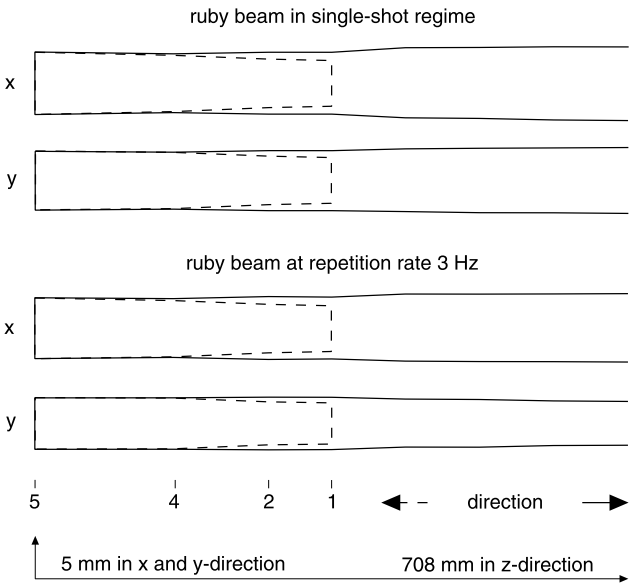

Fig. 4 Schematic representation of the beam caustics of ruby laser in two regimes of operation. The numbers designate the positions of the cavity elements that are shown in Fig. 1

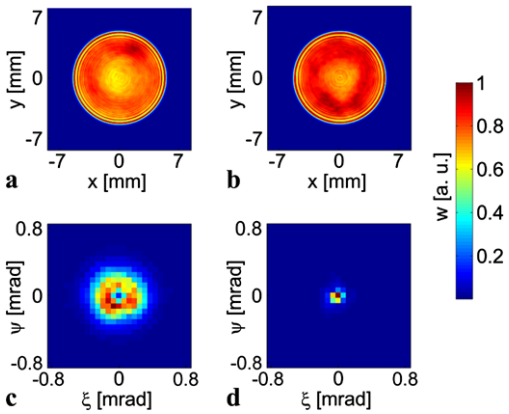

Fig. 5 Calculated beam profiles for Nd:YAG considering the thermal lens effect. (**a**) Near-field in the single-shot regime. (**b**) Near-field at the repetition rate of 5 Hz. (**c**) Far-field in the single-shot regime. (**d**) Far-field at 5 Hz

the single-shot regime (Fig. 5c). With increasing repetition rate the profile is becoming increasingly squeezed due to the positive thermal lens. Finally this leads to the profile shown in Fig. 5d.

The magnification of the ruby cavity is about 1.3 and the coordinates in g-space are (1.16, 0.94), and both are again insensitive to the pumping power. But in contrast to Nd:YAG the astigmatism of thermal lensing in ruby rod operated at 1–5 Hz is very profound. The calculated beam is shown in Fig. 6 for a single shot and for two repetitive regimes. The thermal lens again predominantly affects the FF profile, but now not only the beam size, but also the beam shape is changing. In the single-shot regime with $f_s = \infty$ and

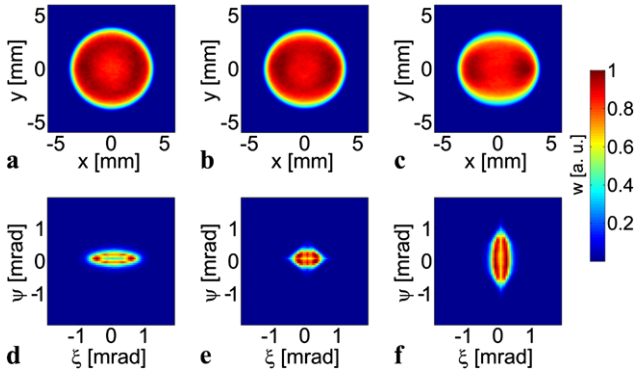

Fig. 6 Calculated beam profiles for ruby considering the thermal lens effect. (**a**) Near-field in the single-shot regime. (**b**) Near-field at the repetition rate of 1 Hz. (**c**) Near-field at 3 Hz. (**d**) Far-field in the single-shot regime. (**e**) Far-field at 1 Hz. (**f**) Far-field at 3 Hz

$f_a = 15$ m the FF profile is first stretched in the ξ-direction, then it becomes circular at $f_s = 40$ m and $f_a = 12$ m, and finally it becomes stretched in the ψ-direction at $f_s = 30$ m and $f_a = 9$ m.

We can explain this as follows: in the absence of any thermal lensing the design of the cavity produces a divergent output beam. The dioptric power of the astigmatic thermal lens increases faster in ψ-direction than in ξ-direction which at first causes beam collimation in the ψ-direction and so the beam is elongated in the ξ-direction. In the mid repetition rate regime this effect overcompensates the divergence in ψ-direction produced by the cavity design and a beam focal point emerges in ψ-direction. Because of this focal point further increase in repetition rate will now result in increasing the divergence in ψ-direction, while in the ξ-direction the divergence is still decreasing. At this point the beam has almost symmetric FF pattern in both directions. At very high repetition rates the astigmatic lens then starts spreading the beam further in both directions. Because the divergence is still increasing faster in the ψ-direction this now results in an elongated beam in the ψ-direction. The NF profile is first unaffected, but becomes squeezed a bit in the y-direction at shorter focal lengths.

3.2 Population lens

In the ruby crystal there is also present a strong electronic population lensing effect. In the calculations we include both the population lens and the thermal lens, and for the latter we used the same set of values for f_s and f_a as in the previous section. The result of the combined thermal and population lensing effects is shown in Fig. 7. By comparing it to Fig. 6 one can see that the population lens distorts both the NF and the FF profiles, however the elongated shape of the FF profiles can be assigned solely to the effects of the astigmatic thermal lens. Generally, the population lensing causes an occurrence of a central dent and a distorted rim in both

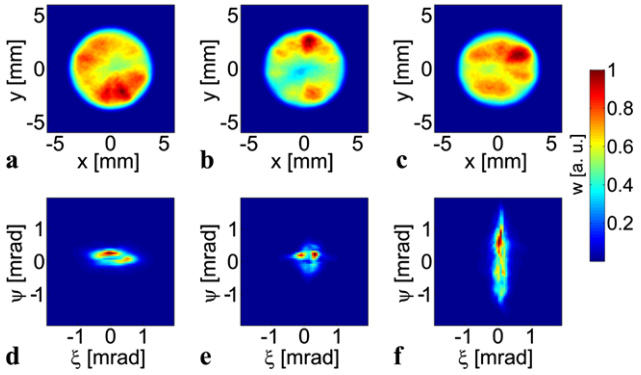

Fig. 7 Calculated beam profiles for ruby with taking into account both the thermal and the population lensing effects. (**a**) Near-field in the single-shot regime. (**b**) Near-field at the repetition rate of 1 Hz. (**c**) Near-field at 3 Hz. (**d**) Far-field in the single-shot regime. (**e**) Far-field at 1 Hz. (**f**) Far-field at 3 Hz

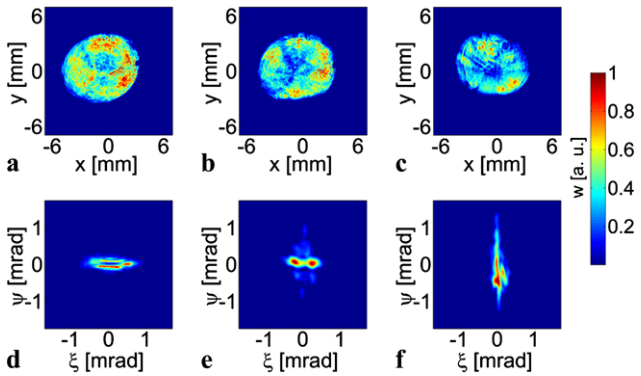

Fig. 8 Measured beam profiles for ruby laser. (**a**) Near-field in the single-shot regime. (**b**) Near-field at the repetition rate of 1 Hz. (**c**) Near-field at 3 Hz. (**d**) Far-field in the single-shot regime. (**e**) Far-field at 1 Hz. (**f**) Far-field at 3 Hz

the NF and the FF profiles. At $f_s = 40$ m and $f_a = 12$ m it splits the FF profile into two peaks in ξ-direction and at $f_s = 30$ m and $f_a = 9$ m it splits the FF into several peaks in ψ-direction. Due to the initial random seed the detailed structures of the NF and FF profiles slightly vary when repeating the calculation, but the main characteristics are well preserved. If we set the values of f_s and f_a below 30 m and 9 m, respectively, the laser operation does not start at all in the simulation.

In order to provide additional quantitative comparison between our numerical results and the measurements we also calculated the beam divergencies θ_ξ^{calc} and $\theta_\psi^{\text{calc}}$ in orthogonal directions. The results are presented in Table 2. The values for the divergencies were obtained from the calculated FF beam shapes using the second-order momentum definition. Because the population lens in ruby causes slightly different results in each run we have taken an average of ten simulation runs for each set of parameters. In addition there is always an error caused by the finite sampling of the EM field. The sampling error was about 0.1 mrad and the calculated standard deviation was smaller than that.

4 Experimental results

We constructed two experimental setups using the two laser crystal rods as described in the previous sections. The flashlamps were powered by a custom-made electric power supply, which provided square-wave pulses of electric power. The Q-switch element was comprised of a polarizer, electro-optic modulator and quarter-wave plate. The polarizer was oriented perpendicularly to the plane defined by the cylinder axis and the crystal axis of the birefringent ruby rod. The beam profiles were measured with a silicon CCD camera having 512 × 512 pixels. To match the detector size the NF profiles were shrank for a factor of 2 with a spherical lens, while the FF profiles were measured in the focal plane of a lens with a focal length of 1228 mm to obtain the required resolution. The beams were appropriately attenuated using a neutral density filter. The divergencies of the beams were determined with a moving knife-edge method and are given in Table 2.

4.1 Ruby

The measured NF and FF profiles for the ruby laser beam are shown in Fig. 8. All the measured profiles agree very well with the calculated profiles from Sect. 3.2. There is a chaotic-type distortion present in the NF profile, i.e. different pattern appears in every single pulse. The FF profile in the single-shot regime is stretched in the ξ-direction, it becomes almost round but split into two peaks at the repetition rate of 1 Hz, and finally it becomes stretched in the ψ-direction at 3 Hz. At higher repetition rates no lasing was observed, which confirms the predictions of our model that strong enough distortions can completely collapse the emergent EM field in the cavity. The measured output beam divergencies are given in Table 2. At repetition rates higher than about 0.9 Hz the quantitative agreement with the numerical results is very good. In the single-shot regime there is a difference of a factor of 2, which is supposed to be due to the rough approximation of the phase factor of the thermal lens in this regime in our model.

4.2 Nd:YAG

The measured NF and FF profiles of the Nd:YAG laser beam are shown in Fig. 9. The NF profile remained constant from single shot up to the 5 Hz repetition of the pump, while the FF profile in single shot showed a central dent that disappeared at 5 Hz, exactly as in the calculated profile (Fig. 5). This confirms our assumption that in Nd:YAG laser systems

Table 2 Calculated and measured divergencies of the output laser beams

Laser	f_s [m]	f_a [m]	Regime	θ_ξ^{calc} [mrad]	$\theta_\psi^{\text{calc}}$ [mrad]	θ_ξ^{meas} [mrad]	$\theta_\psi^{\text{meas}}$ [mrad]
Nd:YAG	∞	∞	single	1.3 ± 0.1	1.3 ± 0.1	1.2 ± 0.1	1.2 ± 0.1
Nd:YAG	22	∞	5 Hz	0.9 ± 0.1	0.9 ± 0.1	0.7 ± 0.1	0.7 ± 0.1
ruby	15	∞	single	2.0 ± 0.1	1.0 ± 0.1	1.41 ± 0.06	0.5 ± 0.1
ruby	40	12	1 Hz	1.2 ± 0.1	0.8 ± 0.1	0.95 ± 0.03	0.9 ± 0.2
ruby	30	9	3 Hz	0.5 ± 0.1	1.4 ± 0.1	0.5 ± 0.1	1.7 ± 0.3

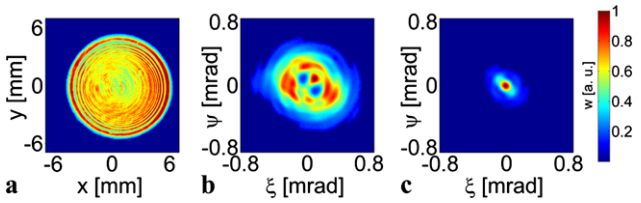

Fig. 9 Measured beam profiles for Nd:YAG laser. (**a**) Near-field in the single-shot regime and at the repetition rate of 5 Hz give practically the same result. (**b**) Far-field in the single-shot regime. (**c**) Far-field at 5 Hz

with unstable cavity design the astigmatic thermal and electronic population lensing effects are negligible. The beam quality is thus limited only by the common spherical thermal lensing effect even though that optical pumping is asymmetric. The measured and the calculated divergencies of the output beam well agree in all operational regimes.

5 Conclusion

In this study we used our numerical model of the laser beam generation to investigate the astigmatism of the thermal lensing effect. This effect was also combined with the electronic population lensing effect in positive-branch unstable laser cavities. By investigating two distinctly different laser media, namely Nd:YAG and ruby crystals, we were able to clearly separate between the contributions related to different origins.

The results show that the astigmatic thermal lensing effect mostly affects the far-field beam profile, while the population lensing effect influences the near-field and the far-field profiles by distorting them in a chaotic manner. In ruby both lensing effects are very expressive, which makes it a very intricate laser medium. On the contrary, in Nd:YAG they are practically negligible, and due to this difference the ruby laser performs much worse than Nd:YAG even when using an optimized cavity.

The numerical results were experimentally validated and were shown to be in excellent agreement for both laser media. Our results demonstrate that such approach can be a powerful tool in the design of some special laser cavities, as for instance in our case the unstable cavity with the super-Gaussian mirror. Our modeling approach can also be easily adapted to other pump and cavity geometries and additional cavity elements can be easily incorporated. We also believe that some of our findings can be further generalized. The astigmatic thermal lensing effects are expected to be important in non-uniformly pumped crystal rods in certain regimes of operation, and the electronic population lensing effects are expected to limit the performance of some transition-metal-ion lasers, e.g. chromium and titanium.

References

1. A.E. Siegman, *Lasers* (University Science Books, Mill Valley, 1986)
2. S. De Silvestri, V. Magni, S. Taccheo, G. Valentini, Opt. Lett. **16**, 642 (1991)
3. F. Brioschi, E. Galletti, M. Garbi, S. Mezzetti, P. Pizzolati, E. Stucchi, Pure Appl. Opt. **3**, 541 (1994)
4. A. Parent, P. Lavigne, Opt. Lett. **14**, 399 (1989)
5. J.F. Pinto, L. Esterowitz, Appl. Opt. **37**, 3272 (1998)
6. A. Caprara, G.C. Reali, Opt. Lett. **17**, 414 (1992)
7. G. Ansett, M. Nittmann, A. Borsutzky, R. Wallenstein, Appl. Phys. B **76**, 833 (2003)
8. W. Koechner, *Solid-State Laser Engineering* (Springer, New York, 2006)
9. W. Koechner, Appl. Opt. **9**, 2548 (1970)
10. X. Wang, Appl. Opt. **46**, 5237 (2007)
11. R. Fluck, M.R. Hermann, L.A. Hackel, Appl. Phys. B **70**, 491 (2000)
12. J. Schwarz, M. Ramsey, D. Headley, P. Rambo, I. Smith, Appl. Phys. B **82**, 275 (2006)
13. X. Zhen, H. Miao, G. Jian-Hong, Z. Zhi-Gan, W. Sha, L. Chong, C. Jun, Chin. Phys. B **18**, 2806 (2009)
14. I. Buske, U. Wittrock, Appl. Phys. B **83**, 229 (2006)
15. K.V. Volodchenko, M.S. Kurdoglyan, C.M. Kim, G.U. Kim, Appl. Opt. **43**, 4768 (2004)
16. M.E. Innocenzi, H.T. Yura, C.L. Fincher, R.A. Fields, Appl. Phys. Lett. **56**, 1831 (1990)
17. J. Frauchiger, P. Albers, H.P. Weber, IEEE J. Quantum Electron. **28**, 1046 (1992)
18. G. Wagner, M. Shiler, V. Wulfmeyer, Opt. Express **13**, 8045 (2005)
19. B. Chen, Y. Chen, J. Simmons, T.Y. Chung, M. Bass, Appl. Phys. B **82**, 413 (2006)
20. D. Pohl, Phys. Lett. A **26**, 357 (1968)
21. A. Flamholz, G.J. Wolga, J. Appl. Phys. **39**, 2723 (1968)
22. K. Ait-Ameur, T. Kerdja, D. Louhibi, J. Phys. D **15**, 1667 (1982)
23. E. Anashkina, O. Antipov, J. Opt. Soc. Am. B **27**, 363 (2010)
24. M. Fromager, K.A. Ameur, Opt. Commun. **191**, 305 (2001)
25. D. Škrabelj, I. Drevensek-Olenik, M. Marincek, IEEE J. Quantum Electron. **46**, 361 (2010)